Available online at www.sciencedirect.com

ScienceDirect

Geochimica et Cosmochimica Acta 270 (2020) 244–263

Geochimica et Cosmochimica Acta

www.elsevier.com/locate/gca

Subsoil organo-mineral associations under contrasting climate conditions

Thiago M. Inagaki [a,d,*], Angela R. Possinger [b], Katherine E. Grant [c], Steffen A. Schweizer [a], Carsten W. Mueller [a], Louis A. Derry [c], Johannes Lehmann [b,d], Ingrid Kögel-Knabner [a,d]

[a] *Chair of Soil Science, Technical University of Munich, Emil-Ramann-Straße 2, Freising 85354, Germany*
[b] *Soil and Crop Sciences, Cornell University, 909 Bradfield Hall, Ithaca, NY 14853, USA*
[c] *Earth and Atmospheric Sciences, 4140 Snee Hall, Cornell University, Ithaca, NY 14853, USA*
[d] *Institute for Advanced Study, Technical University of Munich, Lichtenbergstraße 2a, Garching 85748, Germany*

Received 3 October 2018; accepted in revised form 21 November 2019; available online 5 December 2019

Abstract

Climate differences can induce profound changes in organo-mineral associations in soils. However, the magnitude of these modifications, whether as a direct effect of climate conditions or an indirect effect through changes in soil mineralogy, are still not fully understood. In this study, we aimed to improve understanding of how climate and resultant changes in soil mineralogy affect subsoil (i.e., 0.4–0.9 m) organo-mineral interactions at the macro- and microscale. A set of subsoil samples were collected throughout an elevation gradient (approximately 1800–2400 mm precipitation year^{-1} and 15–24 °C) on Kohala Mountain, Hawaii. We carried out a combined approach of bulk soil analyses with mineral extractions and spectroscopic and spectromicroscopic analyses. Significant positive correlations ($p < 0.05$) between soil organic carbon (SOC) with extracted Fe and Al (dithionite citrate bicarbonate – DCB and ammonium oxalate – OX) at the bulk soil scale supported prior research showing concurrent decline of subsoil Fe, Al and SOC above a precipitation level of ~2000 to ~2200 mm year^{-1}. However, divergence in microscale organo-mineral associations identified using NanoSIMS allowed us to discern the relative roles of Fe and Al in promoting organo-mineral associations. At the lower precipitation range (~1800 mm year^{-1}), the clay fraction < 2 μm showed higher amounts of organic matter (OM) co-localized with Fe & Al compared with the higher precipitation level (~2300 mm year^{-1}), where OM was mostly unassociated or only associated with Al. While Fe contributed to approximately 40% of the microscale organo-mineral associations in the lower precipitation site (quantified by co-localizations with OM segments), this contribution at the higher rainfall regime was only 5%. In contrast, the contribution of Al was approximately the same in both rainfall levels (approximately 30%). Therefore, associations with Al may be more important than Fe for OM stabilization under reducing climate conditions. The normalized CN:C ratio based on individual pixels was found to be higher when co-localized with Al, Fe, or both, especially under the high precipitation regime. This fact points towards the importance of Fe and Al to stabilize more N-rich OM, especially at high rainfall levels. In addition, subsoil from higher rainfall conditions exhibited more reduced forms of Fe (assessed by Fe K-edge XANES) and lower proportions of carboxyl-C (5% lower in the relative abundance) as well as higher alkyl/O-alkyl ratios determined by CP-MAS ^{13}C NMR. Such differences in composition may directly influence the organo-mineral associations at both locations, as differences in Fe reduction and the presence of carboxyl-C groups are recognized to play a role in OM stabilization. We conclude that spatial relationships between Fe and Al with SOC at the microscale show a shift towards Al-dominated SOC associations at higher precipitation

Abbreviations: SOC, soil organic carbon; DCB, dithionite citrate bicarbonate; OX, ammonium oxalate

* Corresponding author at: Chair of Soil Science, Technical University of Munich, Emil-Ramann-Straße 2, Freising 85354, Germany.
E-mail address: thiago.inagaki@wzw.tum.de (T.M. Inagaki).

https://doi.org/10.1016/j.gca.2019.11.030

that could not be ascertained from bulk measurements alone. Therefore, they are of fundamental importance to understand the impact of climate change on SOC stabilization.

Keywords: Fe; Al; Short-range order minerals; Andosols; Organo-mineral interactions

1. INTRODUCTION

Soils have the capacity to store more organic carbon than the global vegetation and atmosphere combined (Lehmann and Kleber, 2015). Therefore, the capacity of soils to foster carbon storage for climate and food security has become increasingly important due to Earth's changing climate (Rumpel et al., 2018). Organo-mineral associations are recognized as one of the most important mechanisms for providing long-term soil organic carbon (SOC) stabilization (Kögel-Knabner et al., 2008). Likewise, soil development and concomitant changes in mineralogy are known to be crucial factors in this process (Harden, 1982). According to Torn et al. (1997), when considering long timescales, changes of mineral-stabilized OC in subsoils provide the largest changes in the quantity and turnover of SOC stocks. Many studies have used proxies of reactive metals, such as Fe and Al extracted by dithionite citrate bicarbonate (DCB), and acid ammonium oxalate (OX) to assess SOC storage potential (Torn et al., 1997; Giardina et al., 2014; Filimonova et al., 2016; Keiluweit et al., 2017). Such phases of minerals are considered essential for the promotion of soil aggregation and SOC protection (Souza et al., 2017). However, the differences in how each element (e.g. Fe and Al) acts in providing SOC stabilization are still unclear. In addition, bulk extractions may not represent the scale at which the organo-mineral associations occur (e.g., micro no nanoscale). Recently, the investigation of microenvironments in soils revealed several novel insights into SOC turnover and sequestration, adding more mechanistic understanding of the measurements performed at the bulk soil scale (Lehmann et al., 2008; Remusat et al., 2012; Mueller et al., 2017; Steffens et al., 2017; Netzer et al., 2018; Pohl et al., 2018; Schweizer et al., 2018; Wiesheu et al., 2018). Although clay size aggregates <2 μm or even smaller fractions are mainly responsible for SOC storage in reactive Fe and Al-rich soils (e.g., Andosols) (Asano and Wagai, 2014), spatially-resolved assessments at the microscale are still relatively rare for studying organo-mineral associations.

In addition, soil moisture stands out as one of five major factors affecting interactions between organic matter and minerals in soil (Kleber et al., 2015). Higher moisture levels promote biological processes, functioning as a solvent for several microbial reactions that enhance organo-mineral associations (Hong et al., 2013). In a recent study, Keiluweit et al. (2017) demonstrated that the formation of anaerobic microsites under higher moisture levels could be an important mechanism for SOC stabilization. On the other hand, excessive moisture promotes loss of SOC from minerals by releasing protected organic matter (Huang and Hall, 2017). It is not yet clear through which mechanisms higher moisture levels can affect organo-mineral interactions in soils. As many studies have already demonstrated, climate change is influencing precipitation amounts and variability worldwide (Trenberth, 2011; O'Gorman, 2015; Madsen et al., 2014). However, most precipitation studies cover large areas, encompassing different biomes and environmental conditions (Trenberth, 2011; O'Gorman, 2015). There are relatively few studies demonstrating the impact of variable climate conditions on mineral associations within soils of similar mineralogy, particularly taking into consideration soil microenvironments.

Here we present a study of mineral-SOC interaction processes across a precipitation gradient of approximately 1800 to 2400 mm year^{-1}. The goal of this study was to understand how different climate conditions impact subsoil organo-mineral associations at the macro- and microscales. We hypothesized that climate-induced changes, either qualitative or quantitative, in association of SOC with reactive metals, especially Fe oxides, are differently expressed between observations at the bulk and microscale.

2. MATERIALS AND METHODS

2.1. Experimental area and soil sampling

The study was carried out in the Kohala region (20°4′14.16″N, 155°43′21.94″E) of northern Hawaii in a rainfall gradient varying from approximately 1800 to 2400 mm year^{-1}, with annual temperatures ranges of 15 to 24 °C, depending on elevation (Giambelluca et al., 2013). The vegetation canopy at the sites changes with elevation. The native vegetation constituted of mixed ohi'a (*Metrosideros polymorpha* Gaudich.) and koai'a (*Acacia koaia* Hillebr.) in the lower part of the transect, grading to a o'hia and mixed fern vegetation at higher parts of the transect (hapu'u - *Cybotium spp.*- and uluhe – *Dicronopteris linearis* Burm.). In the 20th century, the mid elevation forest (up to 1400 m at this site) was largely cleared and replaced by kikuyu pasture grasses (*Pennisetum clandestinum* Hochst.).

We used eleven sites in this study along the climate gradient, six collected from grassland and five from forest vegetation (*Metrosideros polymorpha*). Soil profiles were excavated by hand and sampled by genetic horizon until approximately 1 m depth. Since the main objective of this study was to evaluate subsoil organic carbon stabilization, we focused mainly on 23 samples from 0.4–0.9 m B subsoil horizons across the rainfall gradient. We also included 23 samples from the respective 0.2 m A topsoil horizons to evaluate the influence of aboveground biomass and

Table 1
Soil samples collected in distinct elevation levels at top and subsoil depths throughout the precipitation gradient at the Pololu lava flow, Kohala Hawaii.

Altitude (m)	Vegetation	Precipitation (mm year^{-1})*	Coordinates		Depths (m)
1176	Grassland	1800	20°3′35.10″N	155°43′56.82″E	0.0–0.05
					0.05–0.25
					0.5–0.7
					0.7–0.9
1251	Grassland	1900	20°3′44.68″N	155°43′45.55″E	0.0–0.15
					0.15–0.25
					0.5–0.9
					0.7–0.9
1416	Grassland	1900	20°3′48.54″N	155°43′35.30″E	0.0–0.15
					0.15–0.25
					0.5–0.7
					0.7–0.9
1361	Grassland	2000	20°4′13.33″N	155°43′30.83″E	0.0–0.05
					0.05–0.25
					0.5–0.7
					0.6–0.7
1388	Grassland	2000	20°4′4.98″N	155°43′33.24″E	0.0–0.10
					0.10–0.16
					0.4–0.6
					0.6–0.8
1409	Grassland	2100	20°4′8.04″N	155°43′31.65″E	0.0–0.12
					0.12–0.20
					0.5–0.7
					0.6–0.8
1429	Forest	2100	20°4′8.36″N	155°43′28.02″E	0.0–0.03
					0.03–0.10
					0.4–0.6
					0.6–0.8
1440	Forest	2100	20°4′5.54″N	155°43′33.24″E	0.0–0.05
					0.05–0.15
					0.4–0.5
					0.5–0.7
1460	Forest	2200	20°4′14.16″N	155°43′21.94″E	0.0 to −0.13
					0.13 to −0.17
					0.4–0.6
					0.6–0.7
1478	Forest	2300	20°4′17.40″N	155°43′18.48″E	0.0 to −0.08
					0.08 to −0.15
					0.4–0.6
					0.6–0.7
1554	Forest	2400	20°4′25.93″N	155°43′13.84″E	0.0–0.10
					0.10–0.17
					0.4–0.6
					0.6–0.7

* Precipitation values were obtained through interpolation between elevation and the different isoheytes in the Hawaii Rainfall atlas (Giambelluca et al., 2013).

vegetation change on topsoil layers. The complete set of samples with respective location and depth can be found in Table 1.

2.2. Soil mineralogy and organic matter distribution along the climate gradient

The soil is characterized as an Andosol derived from alkalic lavas of the 350 ka Pololu basalt that likely also received ash deposition from the younger (150 ka) Hawi basalt series (Wolfe and Morris, 1996). The soils were sieved (4-mm mesh). In order to maintain field-moist conditions, we kept the samples in boxes with ice bags while they were transported to the laboratory and stored in climate-controlled rooms at 4 °C. All analyses (in Section 2.2) were performed in duplicate and the results were corrected by the respective moisture level of each sample. Soil organic carbon contents were measured by dry combustion (CHNSO Elemental Analyzer, Hekatech, Wegberg – Germany). Due to the high rainfall regime and soil pH < 7, ($CaCl_2$),

no pre-treatment for carbonate removal was necessary. Pre-tests conducted with 1 M HCl solution also demonstrated no reaction in the samples.

We determined what we call proxy for "reactive metals" in this study, which refers to Fe and Al extractable from soil by selective dissolution techniques of acid ammonium oxalate and citrate-dithionite. These reactive phases include monomeric metal cations related to organic ligands, short-range order minerals such as allophane- and imogolite-type minerals, amorphous metal phases, and minor fractions of crystalline Fe oxides, hydroxides and oxyhydroxides (Parfitt and Childs, 1988; Thompson et al., 2011; Levard et al., 2012; Wagai et al., 2018).

We performed extractions of Fe and Al in parallel with dithionite-citrate following the method of Mehra and Jackson (1958) and with NH_4 oxalate at pH 3 according to the method described by Schwertmann (1964). Soil pH was measured in 0.01 M $CaCl_2$ solution (1:2.5 soil:solution ratio) using a pH meter (Orion Star A111, ThermoFisher Scientific, Waltham – MA, USA) and exchangeable Ca, Mg, and K were extracted using the NH_4OAc method at pH 7 (Lavkulich, 1981). All the extracted elements were measured by inductively coupled plasma optical emission spectroscopy (ICP-OES) (Vista-Pro CCD simultaneous, Varian, Darmstadt - Germany). In addition, we analyzed the mineralogy of the fine clay fraction (<2 μm) (Section 2.3) by X-ray diffraction (PW 1830, Phillips, Amsterdam - Netherlands; X-ray source: Co K alpha).

2.3. Fe speciation by Iron K-edge X-ray Absorption Near Edge Structure (XANES) spectroscopy

To assess the presence of reducing conditions at higher precipitation levels, we performed Fe K-edge XANES measurements at the Cornell High Energy Synchrotron Source (CHESS) F3 beamline on two bulk subsoil samples of approximately 2200 and 2300 mm precipitation $year^{-1}$, respectively. The F3 beamline uses a hard-bend magnet source with a silicon (111) monochromator tunable to hard X-ray energies (6–18 keV) and a silicon drift X-ray detector. Data were collected for the Fe K-edge in fluorescence mode, with a spot size of approximately 0.5 × 4 mm. The F3 end station is operated at room temperature and under ambient pressure. The Fe K-edge (E_0) was set to 7.112 keV (Prietzel et al., 2007), and scans were collected for the pre-edge region (6.912–7.092 keV) with 0.005 keV step size and 1 s dwell time. For the near-edge (7.092–7.142 eV) region we used a 0.001 keV step size and 2 s dwell time. Multiple scans were collected for each sample; specifically, we collected 2–3 scans for Fe standards and 5 scans for soil samples. Elemental Fe foil was used to collect simultaneous Fe K-edge alignment measurements for each scan.

Fe-organic complex standards (previously published in Bhattacharyya et al. (2018)) included Fe (III) EDTA, Fe (III) citrate, and Fe (II) citrate. Commercially obtained mineral standards include elemental Fe^0 (energy calibration), goethite, and fayalite. All the ssamples, including the standards, were stored air-dry prior to XAS analysis. Additionally, Fe^{2+}-substituted nontronite and ferrihydrite were prepared for this experiment following standard protocols. Briefly, structural Fe^{3+} in nontronite was reduced using the dithionite method described by Stucki et al. (1984). Fe^{2+}-substituted nontronite was stored in an anaerobic environment in ultrapure water suspension prior to XAS analysis. Ferrihydrite ($Fe^{3+}_2O_3$š$0.5H_2O$) was prepared by titration of Fe (III) nitrate (0.005 M) by addition of base (0.05 M KOH) to pH 7 and purification by dialysis (1000D MWCO) and subsequent rinsing and re-suspension in water until XANES analysis (modified from Schwertmann and Cornell (2008)). Samples were prepared for XANES measurements by deposition of ~2.5 g material on polyimide tape (1-mil) thickness. Reduced Fe samples were prepared and stored anaerobically prior to analysis.

Initial processing of scans was completed using Athena in Demeter v. 0.9.25 (Ravel and Newville 2005). Scans were flattened and third-order normalization was performed with a pre-edge normalization range of −150 to −30 eV and post-edge range of +150 to ~400 eV relative to $E_0 = 7112$. Energy calibration was performed for individual scans with reference Fe foil, and aligned scans were merged. The pre-edge centroid and white line energy positions for the normalized probability of X-ray absorbance (μ(E)) were determined by using the peak detection function in Fityk v 0.9.8 (Wojdyr, 2010) for energy ranges of 7110–7118 eV (pre-edge centroid) and 7119–7160 eV (white line). The Fe K-edge position (E_0) (i.e. the edge inflection point) was identified by the maximum of the first derivative of normalized μ(E).

Additionally, the relative contribution of Fe^{2+} to the total Fe XANES spectrum was described using the first derivative of normalized μ(E). In the first derivative μ(E) spectrum, the area of the peak assigned to the 1 s–4 s transition (~7120 eV) can be used to estimate relative Fe^{2+} (Berry et al., 2003). The ~7120 eV peak area relative to total area was determined by fitting four Gaussian functions at 7112, 7120, 7124, and 7128 eV to the first derivative μ(E) over the range >7100 and <7140 eV using the Levenberg-Marquadt algorithm in Fityk v 0.9.8. (Wojder, 2010), with the function at 7120.0 eV fixed and the remaining functions constrained by ±3 * sin(~0) eV. Peak full-width half-maximum was constrained to 2 ± 1 * sin(~0) eV and peak height was unconstrained. The fitted area of the 7120 eV peak was divided by the sum of all four-peak areas to determine relative contribution to the total XANES spectrum.

2.4. Isolation of clay-sized fraction

In order to obtain a pure clay-sized fraction that was free of particulate organic matter, we performed clay isolation. The separation of the clay-sized fraction allows studying the organo-mineral associations at the micrometer scale without the interference of other components that are not directly associated with soil mineral surfaces.

The procedure was adapted from the soil organic matter fractionation method described by Golchin et al. (1994), using 4-mm sieved soils under field-moist conditions. In our tests for choosing an isolation method, we assessed

three different approaches to disperse the soil: (1) using a 1 M NaCl solution, (2) using deionized water, and (3) using a sodium polytungstate solution (density of 1.8 g cm^{-3}). Overall, no differences were observed regarding the SOC distribution using the different solutions (Inagaki et al., 2019). This was mainly a result of the fact that the subsoil samples analyzed in our study contained an insignificant amount of particulate organic matter (less than 1% of the total SOC amount). Therefore, we opted to proceed using deionized water for clay separation. The complete procedure is described as follows.

First, we gently saturated the soil by adding deionized water yielding a suspension of 1:2.5 soil:water volume. For the dispersion of macroaggregates and larger microaggregates, we utilized ultrasonic dispersion (SonopulsHD2200, Bandelin, Berlin - Germany) with an energy input of 1500 J ml^{-1}. This energy level is considered sufficient for providing dispersion of the highly stable Andosol microaggregates without causing damage to the primary mineral structure (Silva et al., 2015). After centrifuging the suspension (8000*g* for 40 min), the floating particulate organic matter was removed from the supernatant using a vacuum pump.

Later, the soil mineral fraction (i.e., free of particulate organic matter) was sieved with a 20-μm sized mesh in order to separate sand and coarse silt-sized fractions. The mineral fraction was then subjected to sedimentation to separate the medium silt and clay-sized fractions of 20–2 μm and <2 μm, respectively. The <2 μm clay-sized fraction was subsequently freeze-dried and used for imaging and ^{13}C NMR spectroscopy.

2.5. Soil organic matter characterization by ^{13}C CP/MAS NMR spectroscopy

Soil clay fractions (<2 μm) of four soil profiles of precipitation levels across the climate gradient were chosen for NMR spectroscopy (approximately 1700, 2000, 2200, and 2300 mm $year^{-1}$, respectively). We performed solid-state ^{13}C NMR spectroscopy (Biospin DSX 200 NMR spectrometer, Bruker, Rheinstetten, Germany) of the <2 μm clay fractions from the subsoil (0.4–0.6 m) with a contact time of 0.001 sec with a pulse delay of 0.4 sec. At least 100,000 accumulated scans were performed. The spectra were integrated using four major chemical shift regions: 0 to 45 ppm (alkyl-C), 45 to 110 ppm (O/N-alkyl-C), 110 to 160 (aryl-C), and 160 to 220 ppm (carboxyl-C) (Knicker and Lüdemann, 1995). Despite the elevated Fe content, no sample pre-treatment with hydrofluoric acid was necessary in order to obtain a well-resolved spectrum.

2.6. Organo-mineral associations at the microscale by Nano scale secondary ion mass spectrometry (NanoSIMS)

Two contrasting samples from lower (approximately 1800 mm $year^{-1}$) and higher (approximately 2300 mm $year^{-1}$) rainfall levels were chosen for NanoSIMS analysis. Before the <2 μm fraction was freeze-dried, we took aliquots from the soil suspension in deionized water. The aliquots of soil suspensions were diluted 20 times in water, pipetted onto a silica wafer and dried in a desiccator at room temperature for subsequent scanning electron microscopy (SEM) and NanoSIMS analysis.

To elucidate the distribution of the mineral particles on the Si-wafer and to choose regions of interests for subsequent NanoSIMS measurements, the samples were assessed by reflected light microscopy (Axio Imager Z2, Zeiss, Oberkochen - Germany) and SEM (JSM 5900LV, JEOL, Tokyo - Japan). Prior to the measurement the samples were coated with Au/Pd (~30 nm; SCD 005 sputter coater, Baltec GmbH, Germany), and during measurements the electron flood gun was used to compensate for any charging effects (Mueller et al., 2013). The NanoSIMS imaging was performed using the NanoSIMS 50L (Cameca, Gennevilliers - France) at the Chair of Soil Science of the Technical University of Munich (TUM), Germany, using a high-energy cesium (Cs^+) ion beam (~1.2 pA). We used electron multipliers with a dead time of 44 ns to detect the following secondary ions: $^{16}O^-$, $^{12}C^-$, $^{12}C^{14}N^-$, $^{27}Al^{16}O^-$ and $^{56}Fe^{16}O^-$. Before the analysis, we removed the gold coating layer using a high primary beam current. The beam was focused onto the sample and secondary ions were ejected from the sample surface with a lateral resolution of ~100 nm. The field of view of the measurements was 20 μm · 20 μm (256 · 256 pixels) and the ion images were acquired using a dwell time of 1 ms per pixel with each 40 planes.

2.6.1. M&M: Multi-channel machine-learning segmentation and image analysis

We corrected the NanoSIMS measurements for electron multiplier dead-time by using the OpenMIMS plugin for Fiji (Gormanns et al., 2012). Sum images were created based on auto-alignment of the $^{16}O^-$ distribution across all 40 planes. To differentiate the elemental distributions at the microscale (Fig. 1b–d) and use these to quantify spatial measures, we performed supervised pixel classifications based on the machine-learning algorithm implemented in Ilastik 1.2 (Sommer et al., 2011). We used the $^{16}O^-$ distribution to differentiate between soil particles and Si wafer and define training areas for the algorithm. The additional presence of $^{12}C^-$ and $^{12}C^{14}N^-$ on these particles was used to determine OM segments (Hatton et al., 2012; Remusat et al., 2012). In this regard, we use the term soil particles to refer to the total distribution of segments classified as mineral or OM. The supervised classification included multiple image features like intensity, texture, and gradient in all isotope distributions. Further details of the data preparation and underlying segmentation processes are described in Schweizer et al. (2018). In addition to the classification into background, mineral, and OM segments, we computed similar supervised classifications including $^{27}Al^{16}O^-$ to determine spatial Al-enriched segments and $^{56}Fe^{16}O^-$ to determine Fe-enriched segments (Fig. 1f, g).

The simple segmentation mask based on $^{16}O^-$, $^{12}C^-$, and $^{12}C^{14}N^-$ (Fig. 1e) was used to quantify the spatial arrangement of individual particle and OM segments. In

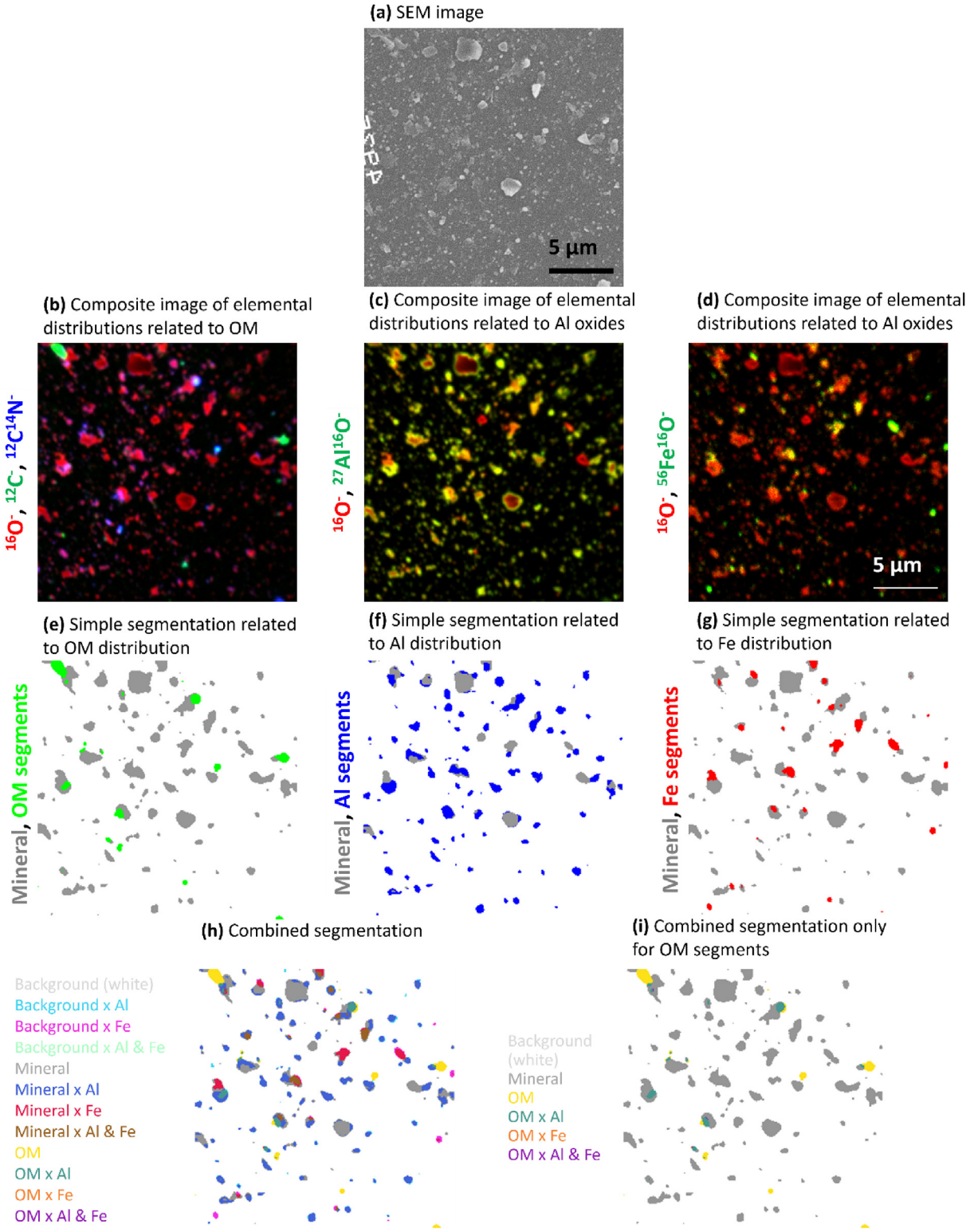

Fig. 1. Workflow of microscale investigations starting with (a) scanning electron microscopy, (b–d) NanoSIMS measurements, (e–g) segmentations based on machine-learning segmentations, and (h, i) combinations of the simple segmentations to more material classes.

total, we detected 333 particles, where 117 were covered by OM, which amounted to 161 OM segments for the soil sample fractionated with H_2O (Appendix, Table A2). We have also performed the same analysis in the clay fraction obtained from the fractionation with NaCl in order to check the data consistency. The latter presented the same trends of the samples fractionated with H_2O and it can be found in the Appendix (Fig. A5, Fig. A6). Particles including less than 5 pixels (0.2 μm^2) were not included in the further analysis. Based on the projected area of particle segments and OM segments, we computed their mean size averaged across all sizes and frequency distributions for the size classes $<0.1\ \mu m^2$, $0.1–0.5\ \mu m^2$, $0.5–2\ \mu m^2$, and $>2\ \mu m^2$. To analyze the relative chemical composition of the OM segments, we determined the normalized CN:C ratio of the individual OM segments based on the simple segmentation mask (Fig. 1e). A higher CN:C ratio indicates a relative increase of N-rich compounds, whereas a lower ratio indicates an increase of C-rich compounds. The relationship of $^{12}C^{14}N^-$:$^{12}C^-$ and $^{12}C^{14}N^-$:$^{12}C^{2-}$ with C:N ratios measured by an elemental analyzer was demonstrated to be linear (Alleon et al., 2015; Hatton et al., 2012).

To quantify the co-localization of OM-, Al-, and Fe-enriched spots, we combined the simple segmentation of mineral and OM segments with the Al and Fe segments into a segmentation mask comprising all possible combinations in 12 material classes (Fig. 1h). To compare the co-localization of OM with Al and Fe, we computed the relative area contributions of the 4 association classes to the total OM segment area (Fig. 1i). By transferring the combined segmentation mask to other isotope distributions, we determined the normalized CN:C ratio across all pixels according to the 4 OM association classes.

2.7. Statistical analysis

We performed linear regression analysis using the R software (R Development Core Team, 2014) to evaluate the relationships between Fe and Al at the bulk soil.

3. RESULTS

3.1. Subsoil mineralogy and organic matter content along the climate gradient

At precipitation levels around 2200 mm $year^{-1}$, our analysis revealed a point at which extracted Fe and Al contents in the subsoil decreased after having achieved maximum levels (Appendix Fig. A1). Similarly, the SOC and N contents did not follow a linear trend as a function of the climate gradient (Appendix Fig. A2) and increased until precipitation reached approximately 2000 mm $year^{-1}$ and decreased above that amount. On the other hand, in the topsoil layers (0–0.2 m), the contents of SOC and N increased along the weather gradient achieving maximum values at the highest evaluated rainfall levels (Appendix Fig. A2). The base saturation (exchangeable Ca, Mg and K) decreased at approximately 2000 mm $year^{-1}$ and then remained the same thereafter, even at the highest precipitation levels. Soil pH was close to neutral (pH = 7) at the lowest rainfall levels and decreased to almost pH 3 at the highest precipitation level. The gravimetric water content increased with measured rainfall from 40 to 80%.

Overall, increases in precipitation promoted decreases in subsoil extractable Fe and Al contents, soil pH, and bases of exchangeable Ca, Mg, and K (Appendix Fig. A1). To evaluate the distribution, we separated the samples into three groups according to precipitation levels. The samples from the lower rainfall level (1800–2000 mm $year^{-1}$) presented higher soil pH values and base content in general. The highest SOC, Fe, and Al concentrations (extracted by DCB and OX) were found at intermediate precipitation levels (2000–2200 mm $year^{-1}$). The samples from the highest rainfall levels (2200–2400 mm $year^{-1}$) can be broadly characterized by a large decrease in soil pH, Fe, and Al contents, and by lower SOC contents. Linear regression analyses between bulk subsoil OC with Fe and with Al (DCB and OX extractable) demonstrated significant relationships ($p < 0.05$) for both mineral proxies (Fig. 2).

3.2. Clay mineralogy and Fe speciation along the climate gradient

The four distinct profiles across the climate gradient had similar soil mineralogy as indicated by the XRD spectra (Appendix, Fig. A3). All soil profiles were characterized by low clay crystallinity. Chlorite and illite, promoted by eolian deposition (Kurtz et al., 2001), were found at higher precipitation levels.

Along the climate gradient, we observed changes in the SOC composition of the clay fraction (<2 μm) as measured by ^{13}C NMR spectroscopy (Fig. 3). Overall, at lower precipitation levels, the samples presented higher relative proportions of carboxyl and O-alkyl-C forms, while samples developed under higher precipitation levels showed higher proportions of alkyl-C. We also observed an increase for the alkyl-C/O-alkyl-C ratio as a function of the precipitation level. As in the case of SOC, Fe, Al, and bases cations, the relative proportion of the carboxyl-C group also decreased above the SOC peak observed at ~2000 mm $year^{-1}$.

While Fe-DCB and Fe-OX decreased by 91 and 93%, respectively, between subsoils from sites receiving 2200 and 2300 mm precipitation $year^{-1}$ (Appendix Fig. A1), descriptive data for normalized Fe K-edge XANES did not show appreciable differences in white line, pre-edge centroid, or inflection point (E_0) for soil samples. Energy shifts in reduced Fe standards (Fe^{2+}-substituted nontronite, fayalite, and Fe(II) citrate) were observed (Appendix, Fig. A4 and Table A1). However, using the area of the 1 s–4 s transition (~7120 eV) peak in the first derivative of normalized μ(E), we identified an increase of reducedFe^{+2} at 2300 vs 2200 mm precipitation $year^{-1}$ (Fig. 4).

3.3. Organo-mineral associations at the microscale observed through NanoSIMS

A supervised classification of the particle and OM segments enabled size comparisons between the precipitation

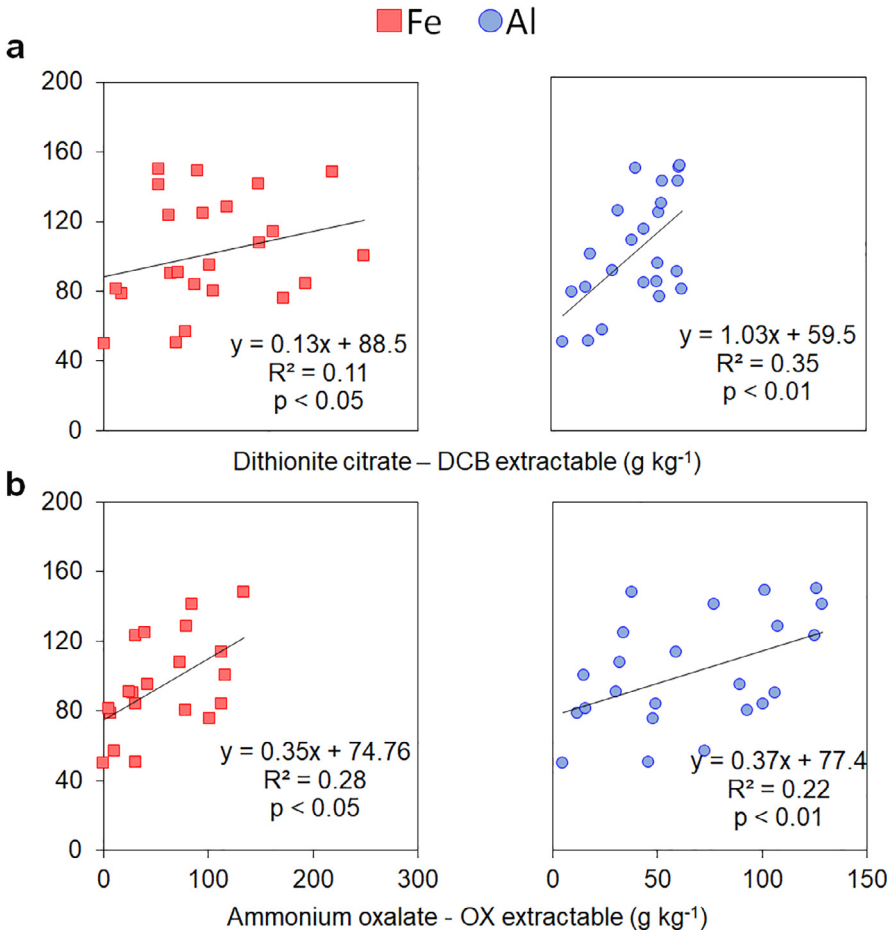

Fig. 2. Relationships between Fe and Al extracted by dithionite citrate (DCB) (a) or ammonium oxalate (OX) (b) and subsoil organic carbon (SOC) of 0.4–0.9 m depths along the precipitation gradient.

regimes. At the low precipitation regime, we found larger particle sizes compared to the high precipitation, whereas the size of the organic matter (OM) segments did not differ (Fig. 5 a,b). In the high precipitation regime, similar-sized OM segments covered smaller particles, which results in a higher coverage of the mineral surfaces. This reveals that the OM was distributed into a larger area on the mineral surface. The normalized CN:C average across individual OM segments was similar between the precipitation regimes, whereas there were contrasting tendencies between the size classes. In the low precipitation regime, the CN:C ratio was higher for OM segments $>0.5\ \mu m^2$ whereas in the high precipitation it was lower for OM segments $>0.5\ \mu m^2$ (Fig. 5c). A similar relationship was shown for the soil fractionated with NaCl (Appendix, Fig. A5c).

By segmenting the OM spots further into associations with Al and Fe, we could compare the two precipitation regimes and quantify distinct properties of co-localized OM associations. Our data revealed more Fe and Fe co-localized with Al on the OM segments under the low precipitation regime compared with high precipitation (Fig. 6a). Al provided the highest area contribution of co-localized OM under the high precipitation regime (Fig. 6a). However, the majority of OM segments were not associated with either Fe or Al under high precipitation (Fig. 6a). A similar relationship was shown for the soil fractionated with NaCl (Appendix, Fig. A6a).

The normalized CN:C ratio based on individual pixels was found to be higher when co-localized with Al, Fe, or both, especially under the high precipitation regime (Fig. 6b). This points towards the interaction of more N-rich OM compounds with Al and Fe. The pixel-based total mean of the CN:C ratio was lower for the high precipitation regime than for the low precipitation regime (Fig. 6b). This is explained by the higher area contributions of the unassociated OM with a generally more C-rich composition (Fig. 6b).

4. DISCUSSION

4.1. Relative role of Fe and Al in promoting organo-mineral associations at the macro and microscale

Our combined approach using extraction and spectro-microscopic techniques revealed that the organo-mineral associations were differently expressed between bulk soil

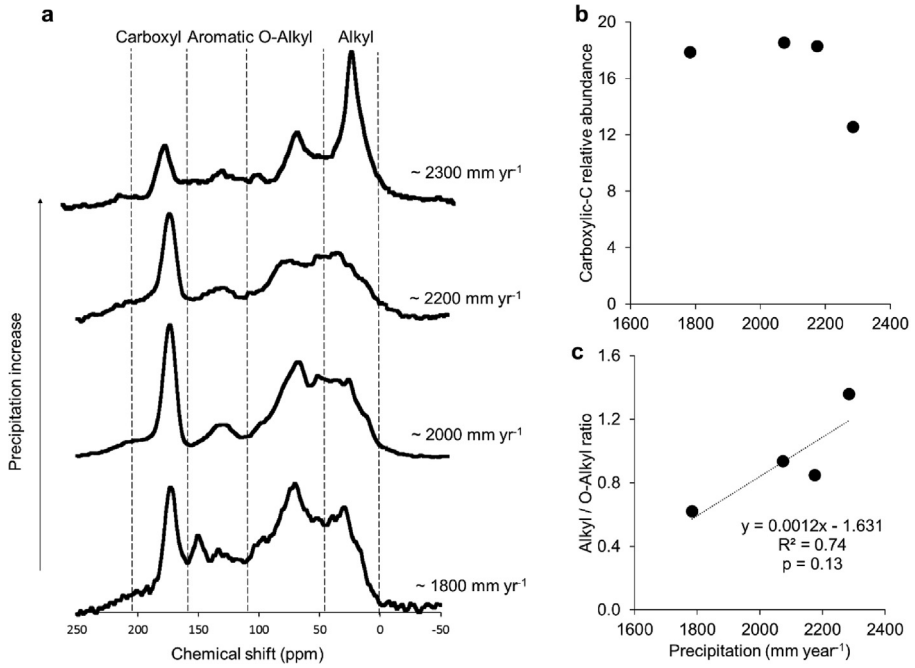

Fig. 3. ^{13}C NMR spectra of the clay fraction (<2 μm) of subsoil samples collected from distinct positions of the climate gradient (a). Decrease of carboxylic-C relative abundance at the higher precipitation level indicates that reducing conditions promote the decrease of this reactive group (b). Increase of alkyl/O-alkyl-C ratio indicates the presence of less oxygenated C forms at higher precipitation levels (c).

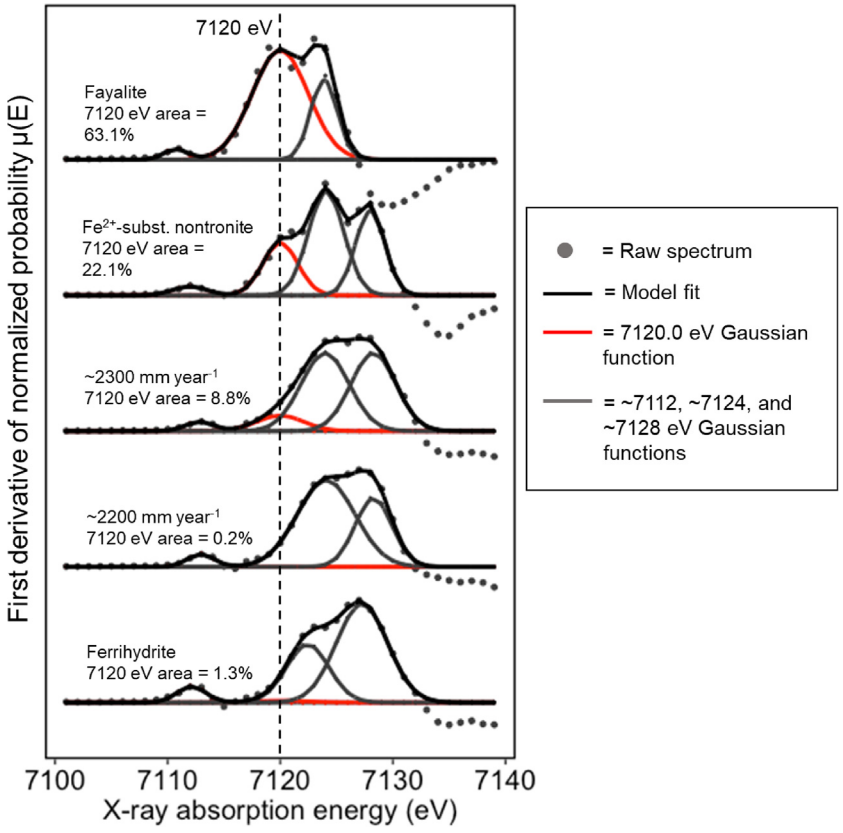

Fig. 4. First derivative of normalized μ(E) iron K-edge XANES spectra for the precipitation levels at 2200 mm year^{-1} and 2300 mm year^{-1}. The Gaussian function at 7120.0 eV (red line) associated with the 1 s–4 s transition (Berry *et al.*, 2003) was used as an estimate of the lower-energy shift of the XANES edge associated with increased Fe^{2+} content, indicating more reduced forms of Fe at higher precipitation levels. Additional reference spectra and model fits are included in Appendix Fig. A4 and Table A1.

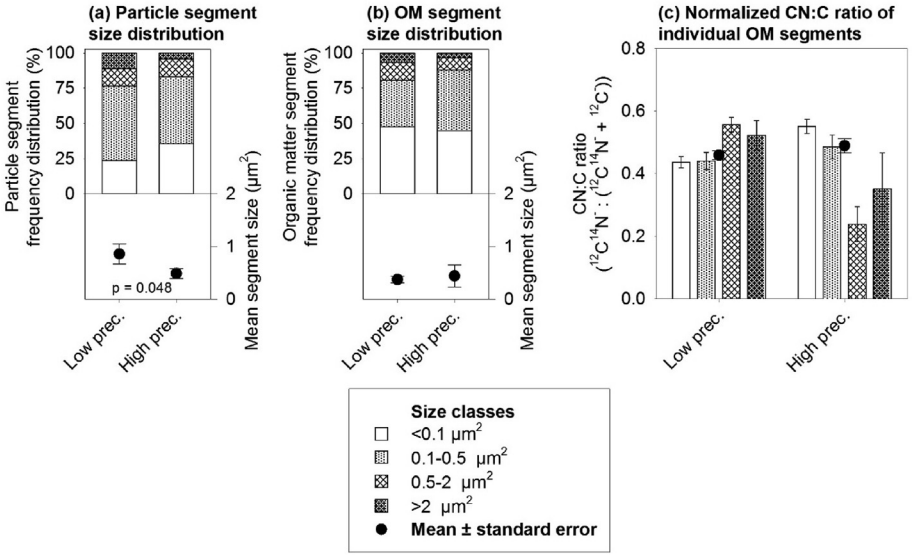

Fig. 5. Microspatial properties in coarse clay fraction fractionated with H_2O. (a, b) Frequency distribution of various size classes and mean size of particles and OM segments (underlying numbers in Appendix Table A6). (c) Mean normalized CN:C ratio and means of various size classes within. The p-value is given in case of significant t-test.

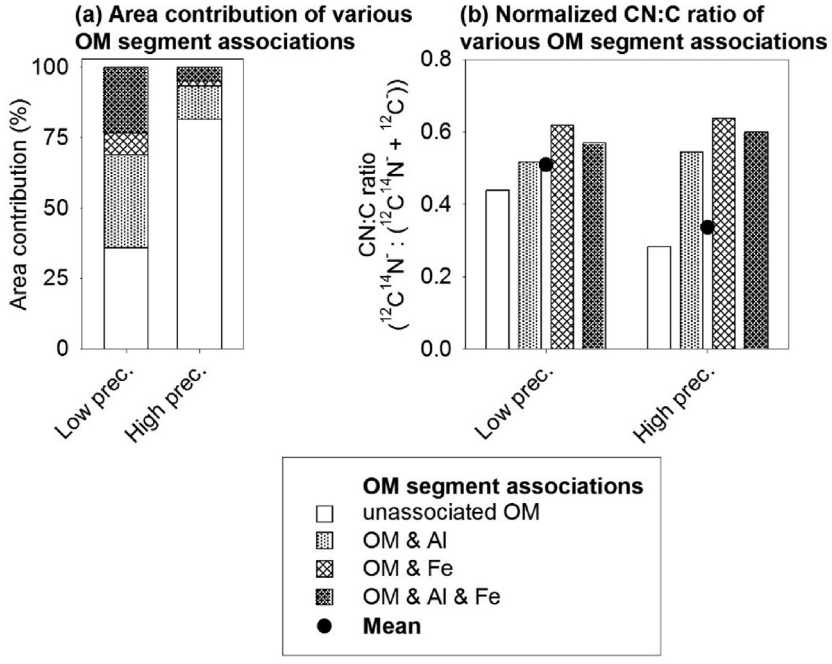

Fig. 6. Microspatial properties in <2 µm clay fraction fractionated with H_2O. (a) Area contributions of OM segment associations. (b) Mean CN:C ratio of all pixels of the various OM segment associations.

and microscale. The relationships between SOC with either pedogenic Fe or Al (e.g. extracted by DCB and OX) along the climate gradient demonstrated the significant role of both proxies for reactive metal oxides in SOC stabilization as supported by several studies (Asano et al., 2018; Basile-Doelsch et al., 2007; Schwertmann, 1964; Torn et al., 1997; Wagai et al., 2018). As Torn et al. (1997) demonstrated in their research, the changes in soil mineralogy play a major role controlling SOC accrual in the Kohala region.

The use of chemical extraction methods is widespread because they are inexpensive and do not demand special laboratory infra-structure (Rennert, 2019). In our study,

they were a useful tool to demonstrate the overall relationship of Fe and Al proxies with SOC at a landscape scale, given the significant correlations (Fig. 2). Comparisons of the relative role of Fe and Al in promoting SOC storage vary according to the region and soil type (Wiesmeier et al., 2019). Overall in Andosols, Al seems to be the main driver as demonstrated by Matus et al. (2006), who concluded that Al extracted by acid ammonium acetate was the principal factor controlling SOC stocks in a series of volcanic soils in Chile. In our study, although we observed slight differences in R^2 and p values between the correlations of DCB extracted Fe ($R^2 = 0.11$, $p = 0.02$) and Al ($R^2 = 0.35$, $p < 0.01$) with SOC (Fig. 2a), these parameters did not show a difference in OX extractions (Fe: $R^2 = 0.28$, $p = 0.01$; Al: $R^2 = 0.22$, $p < 0.01$) (Fig. 2b). Hence, the relative importance of both elements could not be ascertained from these bulk soil measurements.

In addition, although the use of extractable reactive metals has been recognized as a good indicator of SOC accrual (Asano and Wagai, 2014; Beare et al., 2014; McNally et al., 2017), this metric may not represent the scale at which organo-mineral association processes occur (i.e., micro to nanoscale). In this context, the different patterns of organo-mineral associations observed through NanoSIMS in our study demonstrate the importance of combined assessments including microscale observations in addition to bulk soil analyses. These combined evaluations were a useful tool to discern the relative importance of Fe and Al in promoting organo mineral interactions. The differences in the area proportions of Fe-OM, Al-OM and Fe & Al-OM demonstrate the influence of climate, especially reducing conditions, on the subsoil organo-mineral associations at the microscale (Fig. 6). In this way, our findings offer insights regarding the influence of this rainfall gradient on soil organo-mineral associations, which can serve as important information to understand the effects of climate change on SOC accrual.

4.2. Mechanisms of organo-mineral associations affected by climate factors

Our results suggest that a major proportion of the organic matter measured by NanoSIMS at higher rainfall levels (~2300 mm $year^{-1}$) is unassociated with Fe and Al (e.g., 80% of the total segmented area), while most of the remaining organo-mineral interactions are Al-OM associations (Fig. 6a). This result highlights the importance of Al in promoting overall SOC stabilization especially at higher precipitation regimes. Since the majority of previous studies on mechanisms of organo-mineral interaction focused on Fe associations (Gu et al., 1994; Saidy et al., 2012; Chen et al., 2014; Chen et al., 2016), we emphasize the importance of directing more attention to mechanisms of Al-SOC associations, especially in areas under high precipitation regimes.

While microscale Al-OM associations contributed to a larger extent to organo-mineral associations at both precipitation regimes, the Fe-OM associations were more affected by climate conditions since they were less important at the higher precipitation regime (Fig. 6A). While Fe contributed to approximately 31% of the microscale organo-mineral associations (i.e., Fe-OM and Fe-Al-OM associations), this contribution at the higher rainfall regime was only 6% (Fig. 6a). On the other hand, the contribution of Al-OM associations was approximately the same at both rainfall levels (i.e., approximately 30%). The stronger spatial Al correlations in comparison to Fe observed at the microscale may be influenced by the elements relative proportion (McNally et al., 2017), since the Al contents were higher, especially at the higher precipitation regime, than Fe contents.

The shift in Fe speciation may also play a role in causing the differing proportions of Fe-OM and Al-OM associations observed in our study. The Fe reduction in montane tropical regions can be mediated by the presence of bacterial communities responsible for Fe reduction as demonstrated by Dubinsky et al. (2010). Our observations of more reduced Fe forms at the higher precipitation levels are in accordance to the findings by Thompson et al. (2011) who observed a decrease of Fe^{3+} oxides as a function of increased rainfall in the Kohala gradient through Mössbauer spectroscopy. Such Fe reduction can potentially result in a loss of SOC to the aqueous phase. Elevated moisture levels can result in SOC losses mainly by its release from Fe associations as demonstrated by Huang and Hall (2017) and Pan et al. (2016) in incubation experiments. According to the authors, this release represents a yet under-appreciated mechanism for SOC destabilization. Similarly, Adhikari and Yang (2015) observed losses of 5 to 44% of C under reducing conditions in an incubation experiment. According to the authors, the persistence of Fe-OM associations can be governed by organic matter chemical composition and molecular-level interactions between Fe and C. These observations agree with the lower proportions of Fe co-localized with OM at the microscale at the wetter site (Fig. 6), demonstrating that the climate conditions at this area decreased Fe-OM association.

The increase in the organic matter Alkyl-C / O-N Alkyl ratio observed through NMR spectroscopy (Fig. 3) and the shift in Fe speciation observed through XANES analysis (Fig. 4) demonstrates that differences in climate affected not only the amounts of Fe and SOC but also their composition. At higher precipitation levels, we found a predominance of more aliphatic forms of C (i.e., alkyl-C), lower levels of reactive C groups (i.e., carboxylic-C) as well as more reduced forms of Fe, which are in accordance to the oxygen limitations from greater prevalence of water saturation (Bartlett and James, 1993; Li et al., 2008).

These changes in soil organic matter composition driven by climate factors may have a direct influence on how organo-mineral associations occur in this gradient. For example, the lower proportion of carboxylic C groups at the higher precipitation level (5% lower in relative abundance, Fig. 3b) may influence organo-mineral associations. Carboxylic C groups play an important role in SOC accrual, since it is responsible for forming associations with

minerals through a variety of interactions mechanisms (e.g., cation exchange, ligand exchange) (Aquino et al., 2011). In addition, reactions between carboxylic-C and the surface of Fe oxides are considered to be a dominant process affecting organo-mineral associations in soils (Gu et al., 1994). Therefore, the lower amounts of carboxylic-C at the wetter sites (Fig. 3b) may explain the lower abundance of Fe-OM associations observed in our microscale analysis (Fig. 6a).

The higher proportion of aliphatic compounds at the higher precipitation range (0.74 higher in Alkyl/O-Alkyl ratio, Fig. 3c) also demonstrates the preservation of this group at wetter sites. Aromatic-C forms are recognized to be preferentially adsorbed to Fe oxides in soil (Kramer et al., 2012). However, Adhikari and Yang (2015) demonstrated that, under reducing conditions, these associations could be easily released, while associations with aliphatic C were more persistent. However, our analysis at the microscale showed that approximately 81% of the measured OM in the <2 μm clay fraction at the higher precipitation regime was not co-localized with Fe and Al, compared to 31% in the lower precipitation rainfall (Fig. 6). This demonstrates that especially interactions of Fe-OM associations may be more important for SOC stabilization at lower precipitation sites in our gradient. Therefore, the preservation of such organic matter forms at the higher rainfall regimes may be more related to intrinsic C properties such as hydrophobicity (Piccolo and Mbagwu, 1999), which can reduce access for degrading enzymes (von Lutzöw et al., 2006), or metabolic constraints unrelated to organic matter forms of the substrate.

In addition, by calculating the normalized CN:C ratio of OM segments, we were able to compare the importance of Fe and Al associations to stabilize N-rich OM under contrasting climate conditions. In our study, most of the N-rich organic compounds were associated with Fe and Al rather than with unassociated OM (Fig. 6b). This fact indicates the stabilization of microbially processed OM, since most of the organic N in soil is derived from living organisms (Geisseler et al., 2009; Geisseler et al., 2010; Knicker, 2004). Likewise, Kopittke et al. (2018) observed that added microbially-derived compounds were preferentially attached to distinct areas of soil mineral surfaces after a one-year incubation. The authors emphasize that differences in mineralogy are important to regulate the sorption of microbial products on mineral surfaces or C-dominated moieties. Therefore, we highlight the relative importance of Fe and Al to promote organo-mineral associations with N rich organic matter, especially at the wetter sites.

4.3. Implications for climate-driven effects on soil pedogenesis

The observed changes in Fe speciation and lower SOC concentrations due to losses to the aqueous solution may be directly related to the soil pedogenesis along the climate gradient. As observed in our results (Appendix, Figs. A1 and A2) and in other studies (Chadwick et al., 2003; Li et al., 2017; Torn et al., 1997; Vitousek and Chadwick, 2013), the SOC and reactive metal contents decrease simultaneously under higher precipitation levels above ~2000 mm year^{-1} in the Kohala Hawaiian gradient. Across climate gradients, SOC contents are mainly driven by an optimum combination of temperature and precipitation (Li et al., 2017). Since the XRD spectra demonstrated few differences along the gradient (Appendix, Fig. A3), the variation of SOC contents appeared to be decoupled from the proportion of semi- or non-crystalline minerals (i.e., both sites are characterized by low clay crystallinity and the presence of amorphous substances) (Kramer and Chadwick, 2016). In this case, the transport of mobile SOC (e.g., colloidal and/or dissolved organic carbon, DOC) through deeper horizons is likely a major driver of pedogenesis at these Andosol sites (Buettner et al., 2014; Marin-Spiotta et al., 2011). In an incubation experiment using soils from the Hawaiian gradient, Buettner et al. (2014) observed that Fe reduction increased DOC content in fractions of <430 nm. According to the authors, this colloidal dispersion of SOC during Fe reduction may be a major process responsible for C migration to deeper horizons. The infiltration of DOC through infilling channels in the soil profile has also been pointed out as an important mechanism of DOC transport at higher precipitation ranges in the Hawaiian gradient (Marin-Spiotta et al., 2011).

The transport of DOC throughout the soil profile at the high precipitation range also points towards the role of Al in promoting the SOC stabilization under conditions of Fe reduction, since Al is recognized for stabilization of DOC in soils (Scheel et al., 2007; Schwesig et al., 2003). This may explain the overall higher importance of Al in promoting organo-mineral associations compared to Fe in the higher precipitation range (Fig. 6a). In this context, changes in soil pH influenced by climate conditions may also have a significant influence on these mechanisms. Scheel et al. (2007) observed that Al-OM precipitates could be up to 28 times less mineralized than a comparable DOC in an acidic forest soil. This mineralization was even lower at pH 3.8 when compared to pH 4 ($CaCl_2$). The authors mention the precipitation of aromatic and high molecular weight structures under lower pH values, which led to more stable precipitates. Such results agree with the low pH values (e.g., close to pH 3 measured in $CaCl_2$, Appendix Fig. A1) found at the higher precipitation ranges (> ~2300 mm year^{-1}). Grybos et al. (2009) observed that increases of soil pH under reducing soil conditions (e.g., from 5.5 to 7.4) can potentially cause organic matter desorption. Therefore, the low pH values found at the higher precipitation site may be an important factor to maintain the SOC levels and the remaining Al-OM interactions (Fig. 6A) at this region.

For our topsoil layers (0–0.2 m), the increase of SOC with increasing elevation is likely driven by a change in vegetation (from pasture to forest), and consequently higher inputs of biomass-C (Torn et al., 1997). On the other hand, such effects of land use change unlikely affect subsoil OC contents, as demonstrated by Kelly et al. (1998) through ^{13}C values of soils formed beneath pastureland and forest. According to the authors, the majority of the subsoil OC (taken at a depth of approximately 0.7 m) is from the pre-pasture forest vegetation. Likewise, Chadwick et al. (2007) demonstrated through ^{14}C radiocarbon analysis that

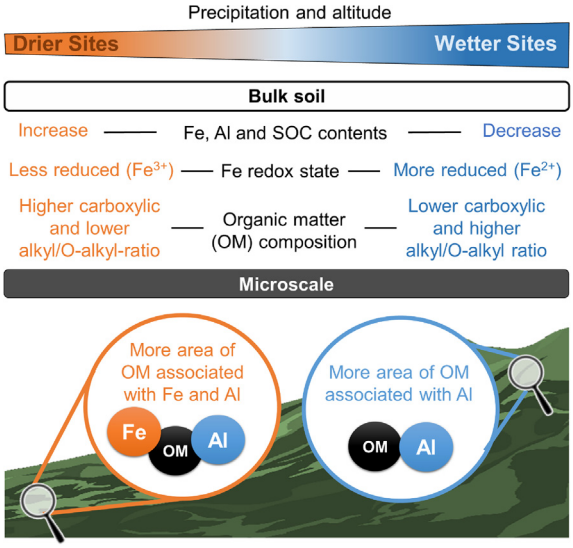

Fig. 7. Conceptual illustration demonstrating the overall effects of climate on soil organo-mineral associations at the macro and microscale in subsoil depths along the climate gradient.

little recent OC has been incorporated into deeper soil horizons following conversion to pasturelands. In addition, in our study, the decreases of SOC contents at higher rainfall levels in the subsoil were observed within the forest area and unrelated to land use change.

Therefore, our results (especially at the microscale) contributes to the overall understanding of the climate influence on soil pedogenesis. In Fig. 7, we demonstrate the overall effects of climate changes on subsoil organo-mineral associations at the macro- and microscale. In this paper, we illustrated under field conditions that the major factors influencing subsoil organo-mineral associations as a function of differences in climate were a combination of lower contents of reactive Fe and changes of Fe and SOC composition. Our results show that the combined use of different quantitative and qualitative techniques at the bulk and micro-scale provide important and complimentary information about how organo-mineral interactions are affected by changing climate conditions.

5. CONCLUSIONS

We have demonstrated that combined approaches at the bulk soil and microscale can provide important information about how subsoil organo-mineral associations are affected by the climate gradient. The observation at the microscale allowed us to disentangle the relative importance of Fe and Al in promoting organo-mineral associations. This information could not be ascertained only from bulk soil measurements. We observed that Al promoted most part organo-Al associations at the higher rainfall regime to a greater extent compared to Fe, which highlights the importance of this element under reducing conditions. We highlight that changes in organic matter composition (i.e., lower carboxylic-C levels) and shift in Fe redox conditions (i.e., to more reduced forms) can affect organo-mineral associations with Fe at higher rainfall levels. We conclude that interactions between reactive metal minerals and SOC at the scale in which mineral interactions occur are of considerable importance to understanding SOC stabilization, and these interactions may not be traceable from analyses at the bulk soil scale. The changes in these associations in subsoils should be taken into consideration when evaluating the impact of climate factors and land use. We recommend that future studies should take the forms of Fe oxides forming at different locations in soil microsites as a function of soil moisture and redox conditions into consideration. In addition, we also encourage researchers to investigate further the overall role of Al in promoting SOC accrual, especially under reducing conditions.

Declaration of Competing Interest

The authors declare that they have no known competing financial interests or personal relationships that could have appeared to influence the work reported in this paper.

ACKNOWLEDGEMENTS

The authors thank the technicians Maria Greiner and Bärbel Angres for their support with the laboratory analysis. Dr. Carmen Höschen for her support with the NanoSIMS measurements. Dr. Rong Huang for his support with data collection at the CHESS F3 end station. Dr. Werner Häusler for his support with the XRD analysis, and the three anonymous reviewers who helped to improve the quality of this manuscript.

FUNDING

This research was supported by the Institute for Advanced Study (IAS) from the Technical University of Munich (TUM) - Germany, through the Hans-Fisher Senior Fellowship. This work uses research conducted at the Cornell High Energy Synchrotron Source (CHESS) which is supported by the National Science Foundation (NSF) - USA, under award DMR-1332208.

APPENDIX A

See Figs. A1–A6 and Tables A1–A3

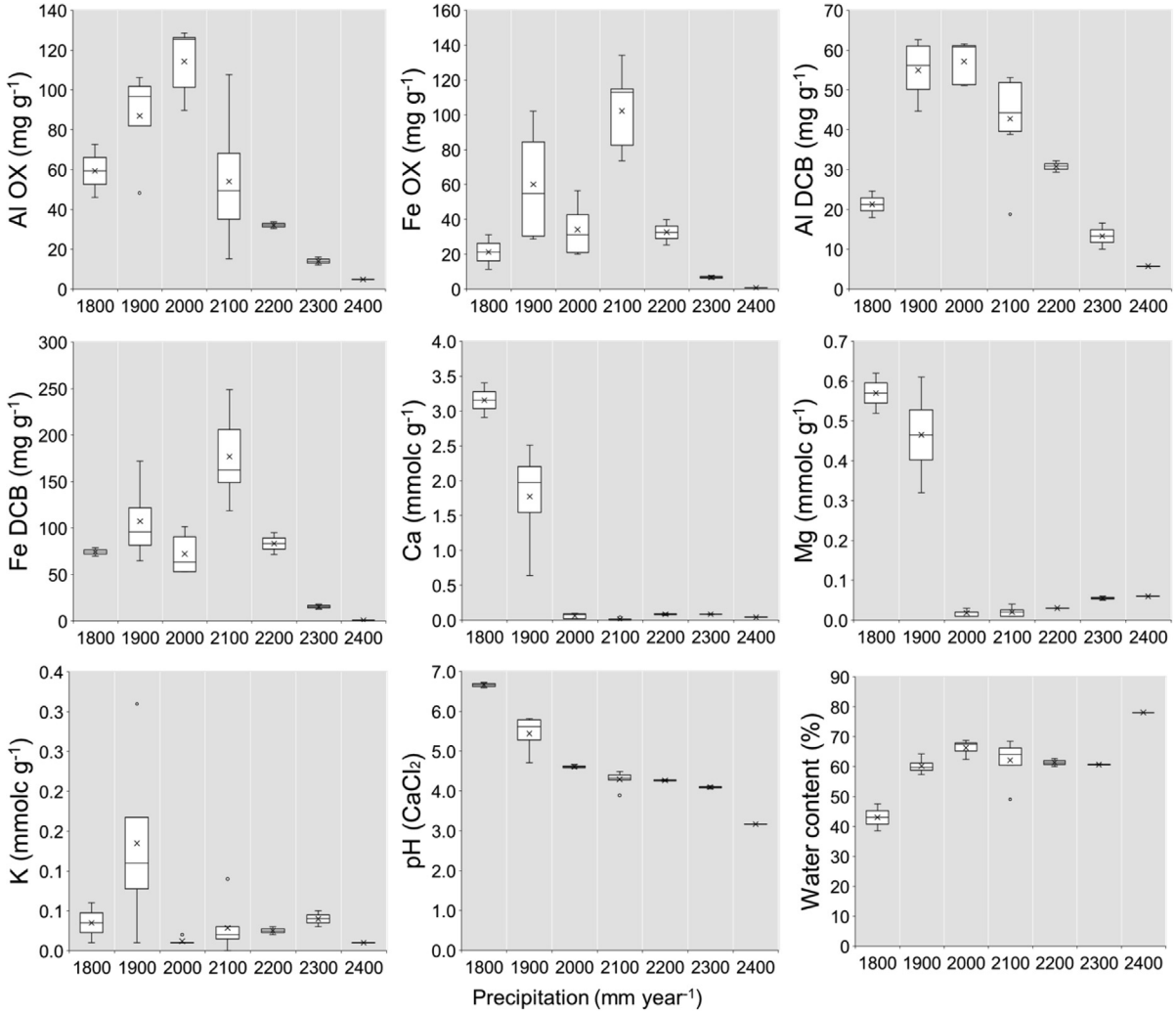

Fig. A1. Fe and Al extracted by dithionite citrate (DCB) and ammonium oxalate (OX); soil pH ($CaCl_2$) and gravimetric water content; and exchangeable Ca, Mg, and K at subsoil depths of 0.6–0.9 m in function of the precipitation gradient (mm $year^{-1}$).

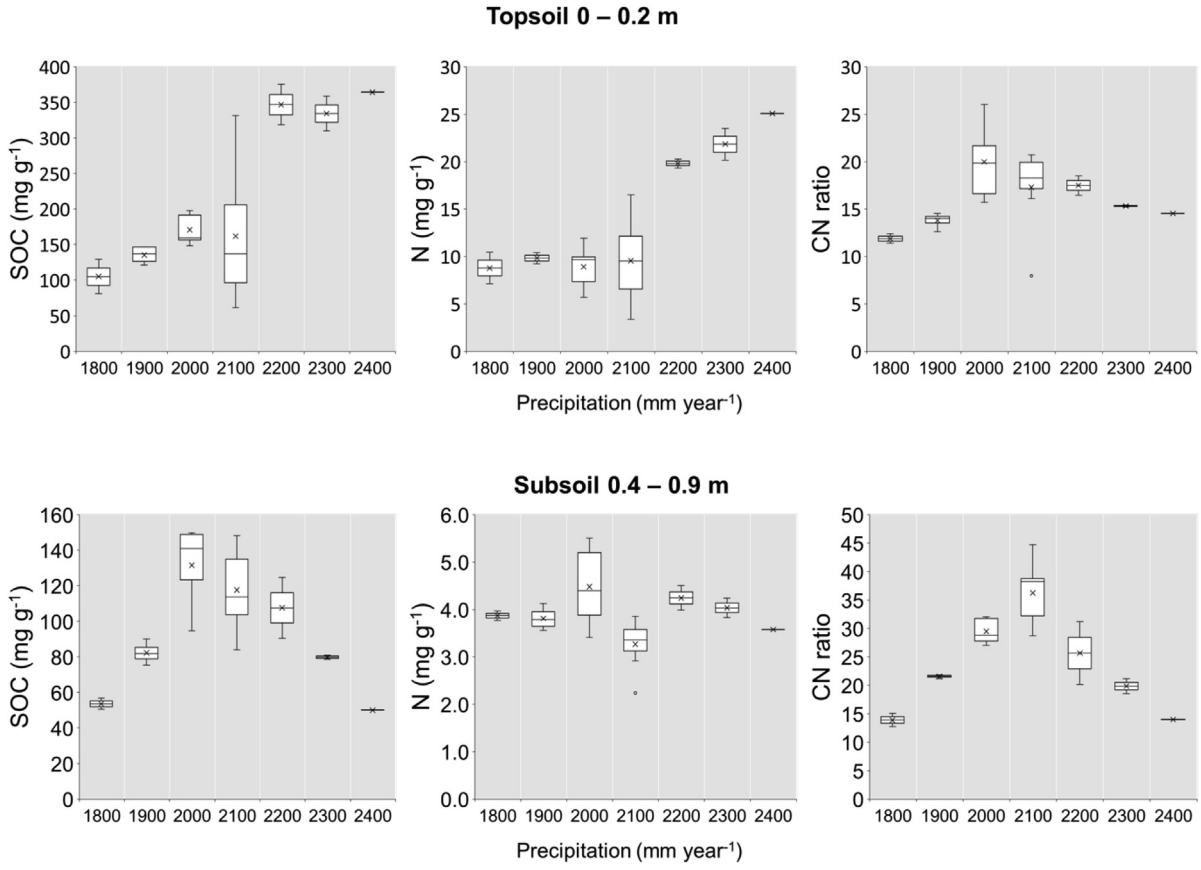

Fig. A2. Soil organic carbon (SOC) and nitrogen (N) contents in topsoils (0–0.2 m) (a) and subsoils (0.4–0.9 m) (b), and C:N ratios in top- and subsoil layers in function of the precipitation gradient (mm year^{-1}).

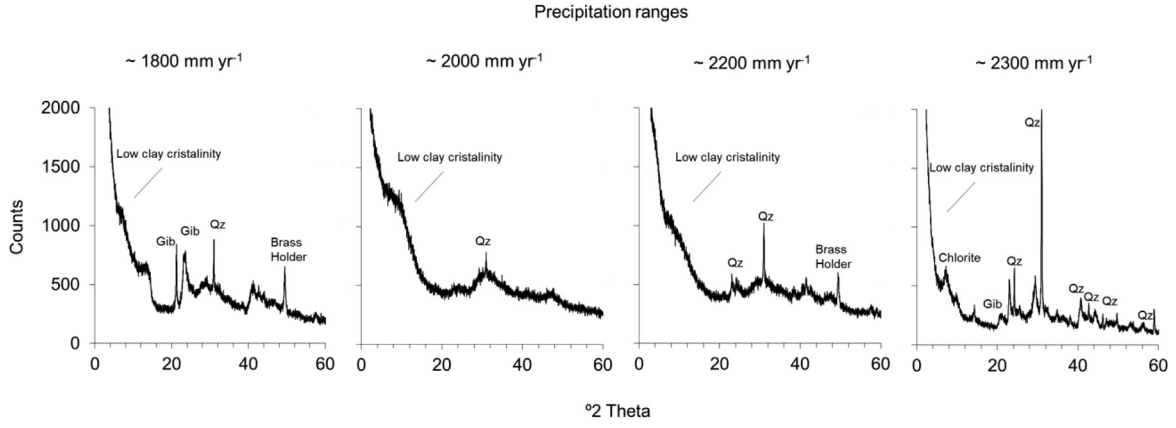

Fig. A3. XRD spectra of the fine clay fraction (<2 μm) of four distinct positions across the rainfall gradient at the depth of 0.4–0.7 m. The "Brass Holder" peak corresponds to the signal that comes from the sample holder, which is made of Brass.

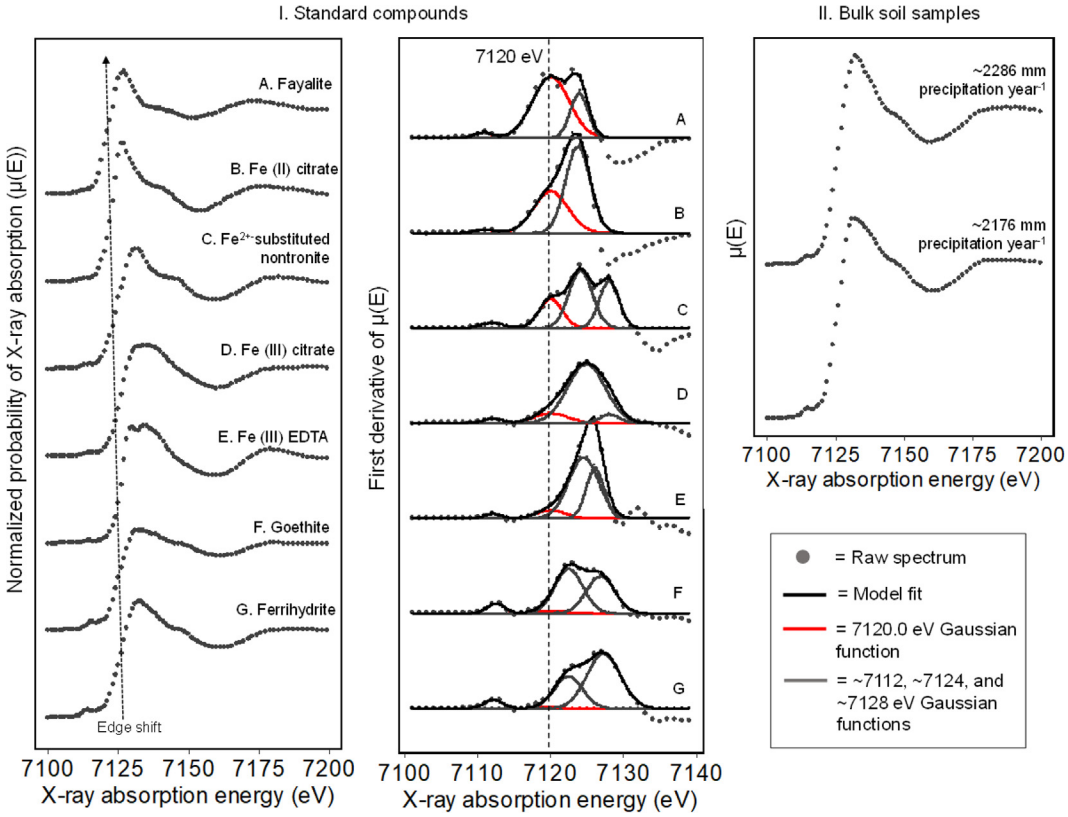

Fig. A4. Normalized probability of X-ray absorbance (μ(E)) for standard compounds and subsoil samples (~2200 and ~2300 mm precipitation year^{-1}), showing energy shifts in pre-edge centroid, edge inflection point, and white line for reduced Fe compounds (Fe^{2+}-substituted nontronite, fayalite, iron (II) citrate). The first derivative of normalized μ(E) shows the increasing contribution of the Gaussian function (red curve) fixed at 7120.0 eV associated with the 1 s–4 s transition as a metric of relative increases in reduced Fe. II. Normalized μ(E) for soil samples, showing no detectable shift in energy position compared to standard compound shifts in I. Values for pre-edge centroid, edge energy (E0), white line energy, and 7120.0 eV peak area are listed in this Appendix in Table A1.

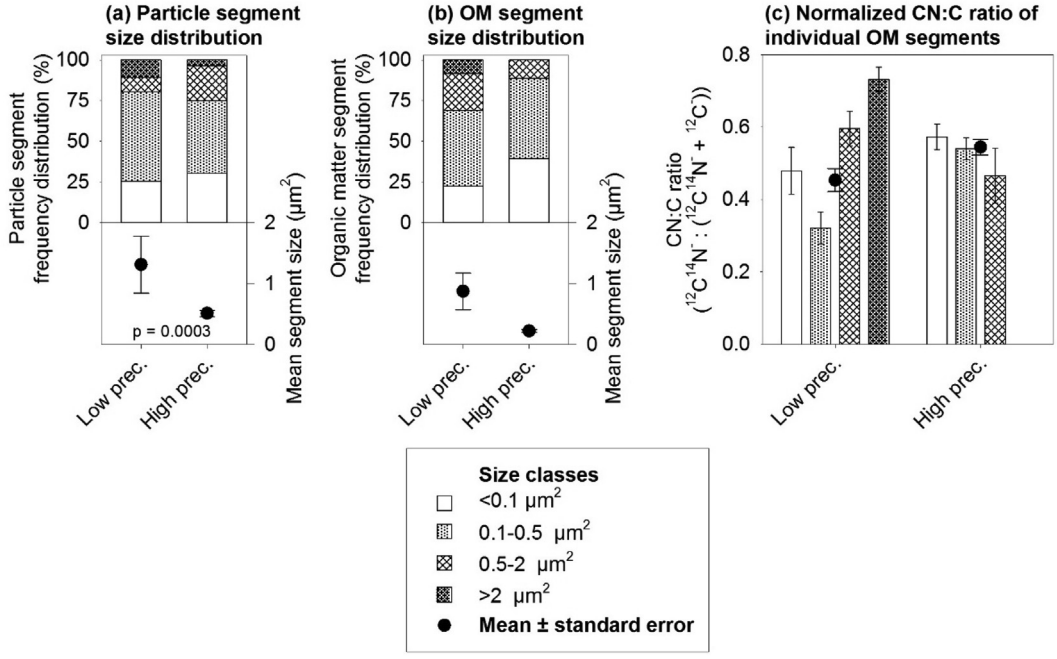

Fig. A5. Microspatial properties in coarse clay fraction fractionated with NaCl. (a, b) Frequency distribution of various size classes and mean size of particles and OM segments (underlying numbers in Table A3). (c) Mean normalized CN:C ratio and means of various size classes within. The p-value is given in case of significant t-test.

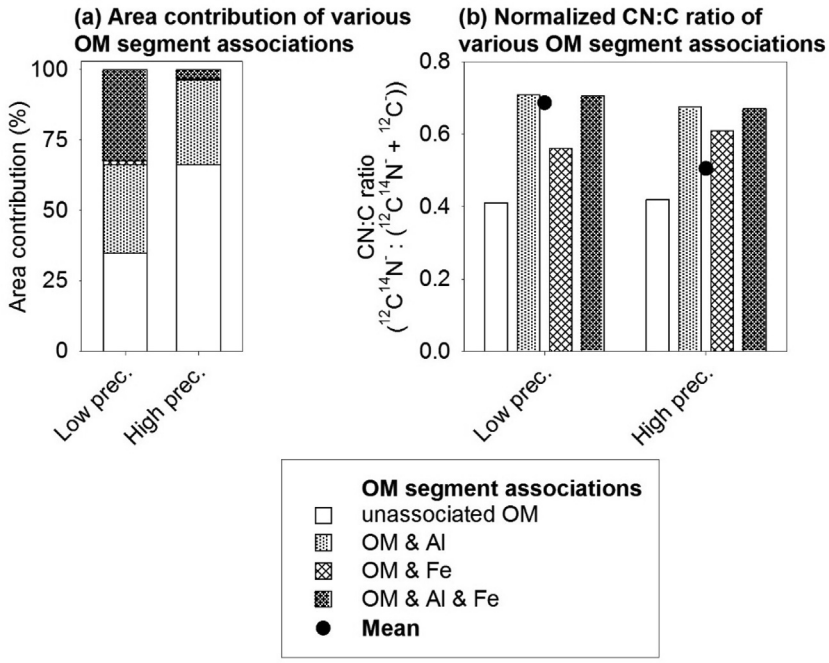

Fig. A6. Microspatial properties in coarse clay fraction fractionated with NaCl. (a) Area contributions of OM segment associations according to the combined segmentations. (b) Mean CN:C ratio of all pixels of the various OM segment associations.

Table A1
Normalized probability of X-ray absorbance (μ(E)) and first derivative of μ(E) descriptive data for soil samples (~2200 and ~2300 mm precipitation year^{-1}) and standard materials with a range of Fe oxidation state.

	Soil Samples		Fe^{3+} minerals		$Fe^{3+}/^{2+}$ mineral	Fe^{2+} mineral	Fe^{3+}-organic complex		Fe^{2+}-organic
	~2200 mm precip	~2300 mm precip	Goethite	Ferrihydrite	Fe^{2+}-nontronite	Fayalite	Fe (III) citrate	Fe (III) EDTA	Fe (II) citrate
Edge (E_0) (eV)	7127	7127	7123	7127	7124	7123	7125	7126	7124
White line (eV)	7132	7132	7131	7133	7131	7127	7134	7134	7126
Pre-edge centroid (eV)	7115	7115	7114	7114	7113	7112	7114	7113	7113
7120.0 peak area (%)	0.23	8.81	3.17	1.28	22.1	63.13	11.81	7.57	39.43

Table A2
Overview on sample and area sizes of microscale investigations using NanoSIMS.

Precipitation	Dispersion	Number of NanoSIMS measurements	Total particle segment area (μm^2)	Total number of particles	Number of particles co-localized with OM	Total OM segment area (μm^2)	Total number of OM segments
Low	NaCl	5	107.5	82	54	62.1	71
High	NaCl	5	155.6	304	88	23.3	104
Low	H_2O	4	84.1	98	68	38.5	103
High	H_2O	4	114.0	235	49	25.5	58

Table A3
Overview on the number of segments in various size classes (Frequency distribution in 5 a, b).

Precipitation	Dispersion	Number of particle segments				Number of OM segments			
		0–0.1 μm^2	0.1–0.5 μm^2	0.5–2 μm^2	>2 μm^2	0–0.1 μm^2	0.1–0.5 μm^2	0.5–2 μm^2	>2 μm^2
Low	NaCl	21	45	7	9	16	33	16	6
High	NaCl	92	136	65	11	41	51	12	0
Low	H_2O	23	52	12	11	49	34	13	7
High	H_2O	83	112	30	10	26	25	5	2

APPENDIX B. SUPPLEMENTARY MATERIAL

Supplementary data to this article can be found online at https://doi.org/10.1016/j.gca.2019.11.030.

REFERENCES

Adhikari D. and Yang Y. (2015) Selective stabilization of aliphatic organic carbon by iron oxide. *Sci. Rep.* **5**, 11214.

Alleon J., Bernard S., Remusat L. and Robert F. (2015) Estimation of nitrogen-to-carbon ratios of organics and carbon materials at the submicrometer scale. *Carbon* **84**, 290–298.

Aquino A. J., Tunega D., Schaumann G. E., Haberhauer G., Gerzabek M. H. and Lischka H. (2011) The functionality of cation bridges for binding polar groups in soil aggregates. *Int. J. Quant. Chem.* **111**, 1531–1542.

Asano M. and Wagai R. (2014) Evidence of aggregate hierarchy at micro- to submicron scales in an allophanic Andisol. *Geoderma* **216**, 62–74.

Asano M., Wagai R., Yamaguchi N., Takeichi Y., Maeda M., Suga H. and Takahashi Y. (2018) In search of a binding agent: nano-scale evidence of preferential carbon associations with poorly-crystalline mineral phases in physically-stable, clay-sized aggregates. *Soil Syst.* **2**, 32.

Bartlett R. J. and James B. R. (1993) Redox chemistry of soils. *Adv Agron* **50**, 151–208.

Basile-Doelsch I., Amundson R., Stone W. E. E., Borschneck D., Bottero J. Y., Moustier S., Masin F. and Colin F. (2007) Mineral control of carbon pools in a volcanic soil horizon. *Geoderma* **137**, 477–489.

Beare M., McNeill S., Curtin D., Parfitt R., Jones H., Dodd M. and Sharp J. (2014) Estimating the organic carbon stabilisation capacity and saturation deficit of soils: a New Zealand case study. *Biogeochemistry* **120**, 71–87.

Bhattacharyya A., Schmidt M. P., Stavitski E. and Martinez C. E. (2018) Iron speciation in peats: Chemical and spectroscopic evidence for the co-occurrence of ferric and ferrous iron in organic complexes and mineral precipitates. *Org. Geochem.* **115**, 124–137.

Buettner S. W., Kramer M. G., Chadwick O. A. and Thompson A. (2014) Mobilization of colloidal carbon during iron reduction in basaltic soils. *Geoderma* **221**, 139–145.

Chadwick O. A., Gavenda R. T., Kelly E. F., Ziegler K., Olson C. G., Elliott W. C. and Hendricks D. M. (2003) The impact of climate on the biogeochemical functioning of volcanic soils. *Chem. Geol.* **202**, 195–223.

Chadwick O. A., Kelly E. F., Hotchkiss S. C. and Vitousek P. M. (2007) Precontact vegetation and soil nutrient status in the shadow of Kohala Volcano, Hawaii. *Geomorphology* **89**, 70–83.

Chen C., Dynes J. J., Wang J. and Sparks D. L. (2014) Properties of Fe-organic matter associations via coprecipitation versus adsorption. *Envir. Sci. Tech.* **48**, 13751–13759.

Chen K.-Y., Chen T.-Y., Chan Y.-T., Cheng C.-Y., Tzou Y.-M., Liu Y.-T. and Teah H.-Y. (2016) Stabilization of natural organic matter by short-range-order iron hydroxides. *Envir. Sci. Tech.* **50**, 12612–12620.

Dubinsky E. A., Silver W. L. and Firestone M. K. (2010) Tropical forest soil microbial communities couple iron and carbon biogeochemistry. *Ecology* **91**, 2604–2612.

Filimonova S., Kaufhold S., Wagner F. E., Hausler W. and Kogel-Knabner I. (2016) The role of allophane nano-structure and Fe oxide speciation for hosting soil organic matter in an allophanic Andosol. *Geochim. Cosmochim. Acta* **180**, 284–302.

Geisseler D., Horwath W. R. and Doane T. A. (2009) Significance of organic nitrogen uptake from plant residues by soil microorganisms as affected by carbon and nitrogen availability. *Soil. Biol. Biochem.* **41**, 1281–1288.

Geisseler D., Horwath W. R., Joergensen R. G. and Ludwig B. (2010) Pathways of nitrogen utilization by soil microorganisms–a review. *Soil. Biol. Biochem.* **42**, 2058–2067.

Giambelluca T. W., Chen Q., Frazier A. G., Price J. P., Chen Y.-L., Chu P.-S., Eischeid J. K. and Delparte D. M. (2013) Online rainfall atlas of Hawaii.B. *Am. Meteoro. Soc.* **94**, 313–316.

Giardina C. P., Litton C. M., Crow S. E. and Asner G. P. (2014) Warming-related increases in soil CO 2 efflux are explained by increased below-ground carbon flux. *Nat. Clim. Chang.* **4**, 822.

Gormanns P., Reckow S., Poczatek J. C., Turck C. W. and Lechene C. (2012) Segmentation of multi-isotope imaging mass spectrometry data for semi-automatic detection of regions of interest. *PloS one* **7** e30576.

Grybos M., Davranche M., Gruau G., Petitjean P. and Pédrot M. (2009) Increasing pH drives organic matter solubilization from wetland soils under reducing conditions. *Geoderma* **154**, 13–19.

Gu B., Schmitt J., Chen Z., Liang L. and McCarthy J. F. (1994) Adsorption and desorption of natural organic matter on iron oxide: mechanisms and models. *Envir. Sci. Tech.* **28**, 38–46.

Harden J. W. (1982) A quantitative index of soil development from field descriptions - examples from a chronosequence in central California. *Geoderma* **28**, 1–28.

Hatton P. J., Remusat L., Zeller B. and Derrien D. (2012) A multi-scale approach to determine accurate elemental and isotopic ratios by nano-scale secondary ion mass spectrometry imaging. *Rapid Commun. Mass Spectrom* **26**, 1363–1371.

Hong Z. N., Chen W. L., Rong X. M., Cai P., Dai K. and Huang Q. Y. (2013) The effect of extracellular polymeric substances on the adhesion of bacteria to clay minerals and goethite. *Chem. Geol.* **360**, 118–125.

Huang W. and Hall S. J. (2017) Elevated moisture stimulates carbon loss from mineral soils by releasing protected organic matter. *Nat. Commun.* **8**, 1774.

Inagaki T. M., Mueller C. W., Lehmann J. and Kögel-Knabner I. (2019) Andosol clay re-aggregation observed at the microscale during physical organic matter fractionation. *J. Plant Nutr. Soil Sc.* **182**, 145–148.

Keiluweit M., Wanzek T., Kleber M., Nico P. and Fendorf S. (2017) Anaerobic microsites have an unaccounted role in soil carbon stabilization. *Nat. Commun.* **8**, 1771.

Kelly E. F., Chadwick O. A. and Hilinski T. E. (1998) The effect of plants on mineral weathering. *Biogeochemistry* **42**, 21–53.

Kleber M., Eusterhues K., Keiluweit M., Mikutta C., Mikutta R. and Nico P. S. (2015) Chapter one-mineral–organic associations: formation, properties, and relevance in soil environments. *Adv. Agron.* **130**, 1–140.

Knicker H. (2004) Stabilization of N-compounds in soil and organic-matter-rich sediments—what is the difference? *Mar. Chem.* **92**, 167–195.

Knicker H. and Lüdemann H. D. (1995) N-15 and C-13 Cpmas and solution Nmr-studies of N-15 enriched plant-material during 600 days of microbial-degradation. *Org. Geochem.* **23**, 329–341.

Kögel-Knabner I., Guggenberger G., Kleber M., Kandeler E., Kalbitz K., Scheu S., Eusterhues K. and Leinweber P. (2008) Organo-mineral associations in temperate soils: Integrating biology, mineralogy, and organic matter chemistry. *J. Plant Nutr. Soil Sci.* **171**, 61–82.

Kopittke P. M., Hernandez-Soriano M. C., Dalal R. C., Finn D., Menzies N. W., Hoeschen C. and Mueller C. W. (2018) Nitrogen-rich microbial products provide new organo-mineral associations for the stabilization of soil organic matter. *Glob. Chang. Biol.* **24**, 1762–1770.

Kramer M. G. and Chadwick O. A. (2016) Controls on carbon storage and weathering in volcanic soils across a high-elevation climate gradient on Mauna Kea, Hawaii. *Ecology* **97**, 2384–2395.

Kramer M. G., Sanderman J., Chadwick O. A., Chorover J. and Vitousek P. M. (2012) Long-term carbon storage through retention of dissolved aromatic acids by reactive particles in soil. *Glob. Chang. Biol.* **18**, 2594–2605.

Kurtz A. C., Derry L. A. and Chadwick O. A. (2001) Accretion of Asian dust to Hawaiian soils: Isotopic, elemental, and mineral mass balances. *Geochim. Cosmochim. Acta* **65**, 1971–1983.

Lavkulich L. (1981) *Methods manual, pedology laboratory*. University of British Columbia, Department of Soil Science, Vancouver, BC, CA.

Lehmann J. and Kleber M. (2015) The contentious nature of soil organic matter. *Nature* **528**, 60–68.

Lehmann J., Solomon D., Kinyangi J., Dathe L., Wirick S. and Jacobsen C. (2008) Spatial complexity of soil organic matter forms at nanometre scales. *Nat. Geosci.* **1**, 238–242.

Levard C., Doelsch E., Basile-Doelsch I., Abidin Z., Miche H., Masion A., Rose J., Borschneck D. and Bottero J.-Y. (2012) Structure and distribution of allophanes, imogolite and proto-imogolite in volcanic soils. *Geoderma* **183**, 100–108.

Li C. L., Cao Z. Y., Chang J. J., Zhang Y., Zhu G. L., Zong N., He Y. T., Zhang J. J. and He N. P. (2017) Elevational gradient affect functional fractions of soil organic carbon and aggregates stability in a Tibetan alpine meadow. *Catena* **156**, 139–148.

Li J., Richter D. D., Mendoza A. and Heine P. (2008) Four-decade responses of soil trace elements to an aggrading old-field forest: B, Mn, Zn, Cu, and Fe. *Ecology* **89**, 2911–2923.

Madsen H., Lawrence D., Lang M., Martinkova M. and Kjeldsen T. R. (2014) Review of trend analysis and climate change projections of extreme precipitation and floods in Europe. *J. Hydrol.* **519**, 3634–3650.

Marin-Spiotta E., Chadwick O. A., Kramer M. and Carbone M. S. (2011) Carbon delivery to deep mineral horizons in Hawaiian rain forest soils. *J. Geophys. Res. Biogeosci.* **116**.

Matus F., Amigo X. and Kristiansen S. M. (2006) Aluminium stabilization controls organic carbon levels in Chilean volcanic soils. *Geoderma* **132**, 158–168.

McNally S. R., Beare M. H., Curtin D., Meenken E. D., Kelliher F. M., Calvelo Pereira R., Shen Q. and Baldock J. (2017) Soil carbon sequestration potential of permanent pasture and continuous cropping soils in New Zealand. *Glob. Chang. Biol.* **23**, 4544–4555.

Mueller C. W., Hoeschen C., Steffens M., Buddenbaum H., Hinkel K., Bockheim J. G. and Kao-Kniffin J. (2017) Microscale soil structures foster organic matter stabilization in permafrost soils. *Geoderma* **293**, 44–53.

Mueller C. W., Weber P. K., Kilburn M. R., Hoeschen C., Kleber M. and Pett-Ridge J. (2013) Advances in the Analysis of Biogeochemical Interfaces: NanoSIMS to Investigate Soil Microenvironments. In *Advances in Agronomy*, Vol. 121 (ed. D. L. Sparks), pp. 1–46.

Netzer F., Mueller C. W., Scheerer U., Gruner J., Kogel-Knabner I., Herschbach C. and Rennenberg H. (2018) Phosphorus nutrition of Populus x canescens reflects adaptation to high P-availability in the soil. *Tree Physiol.* **38**, 6–24.

O'Gorman P. A. (2015) Precipitation extremes under climate change. *Curr. Clim. Change Rep.* **1**, 49–59.

Parfitt R. and Childs C. (1988) Estimation of forms of Fe and Al-a review, and analysis of contrasting soils by dissolution and Mossbauer methods. *Soil Res.* **26**, 121–144.

Piccolo A. and Mbagwu J. S. (1999) Role of hydrophobic components of soil organic matter in soil aggregate stability. *Soil Sci. Soc. Am. J.* **63**, 1801–1810.

Pohl L., Kolbl A., Werner F., Mueller C. W., Hoschen C., Hausler W. and Kogel-Knabner I. (2018) Imaging of Al/Fe ratios in synthetic Al-goethite revealed by nanoscale secondary ion mass spectrometry. *Rapid. Commun. Mass Spectrom.* **32**, 619–628.

R Development Core Team, (2014) R: a language and environment for statistical computing. Vienna, Austria: R Foundation for Statistical Computing; 2012. Open access available at: http://cran.r-project.org.

Remusat L., Hatton P.-J., Nico P. S., Zeller B., Kleber M. and Derrien D. (2012) NanoSIMS study of organic matter associated with soil aggregates: advantages, limitations, and combination with STXM. *Environ. Sci. Technol.* **46**, 3943–3949.

Rennert T. (2019) Wet-chemical extractions to characterise pedogenic Al and Fe species–a critical review. *Soil Res.* **57**, 1–16.

Rumpel C., Lehmann J. and Chabbi A. (2018) '4 per 1,000'initiative will boost soil carbon for climate and food security. *Nature* **553**, 27-27.

Saidy A., Smernik R., Baldock J., Kaiser K., Sanderman J. and Macdonald L. (2012) Effects of clay mineralogy and hydrous iron oxides on labile organic carbon stabilisation. *Geoderma* **173**, 104–110.

Scheel T., Dörfler C. and Kalbitz K. (2007) Precipitation of dissolved organic matter by aluminum stabilizes carbon in acidic forest soils. *Soil Sci. Soc. Am. J.* **71**, 64–74.

Schweizer S. A., Hoeschen C., Schluter S., Kogel-Knabner I. and Mueller C. W. (2018) Rapid soil formation after glacial retreat shaped by spatial patterns of organic matter accrual in microaggregates. *Glob. Chang. Biol.* **24**, 1637–1650.

Schwertmann U. (1964) Differenzierung der Eisenoxide des Bodens durch Extraktion mit Ammoniumoxalat-Lösung. *J. Plant Nutr. Soil Sci.* **105**, 194–202.

Schwertmann U. and Cornell R. M. (2008) *Iron oxides in the laboratory: preparation and characterization*. John Wiley & Sons.

Schwesig D., Kalbitz K. and Matzner E. (2003) Effects of aluminium on the mineralization of dissolved organic carbon derived from forest floors. *Eur. J. Soil Sci.* **54**, 311–322.

Sommer C., Straehle C., Koethe U. and Hamprecht F. A. (2011) Ilastik: Interactive learning and segmentation toolkit. In *2011 IEEE international symposium on biomedical imaging: From nano to macro*. IEEE, pp. 230–233.

Souza I. F., Archanjo B. S., Hurtarte L. C., Oliveros M. E., Gouvea C. P., Lidizio L. R., Achete C. A., Schaefer C. E. and Silva I. R. (2017) Al-/Fe-(hydr) oxides–organic carbon associations in Oxisols—From ecosystems to submicron scales. *Catena* **154**, 63–72.

Steffens M., Rogge D. M., Mueller C. W., Hoschen C., Lugmeier J., Kolbl A. and Kogel-Knabner I. (2017) Identification of distinct functional microstructural domains controlling C storage in soil. *Environ. Sci. Technol.* **51**, 12182–12189.

Stucki J. W., Golden D. and Roth C. B. (1984) Preparation and handling of dithionite-reduced smectite suspensions. *Clays Clay Miner.* **32**, 191–197.

Thompson A., Rancourt D. G., Chadwick O. A. and Chorover J. (2011) Iron solid-phase differentiation along a redox gradient in basaltic soils. *Geochim. Cosmochim. Acta* **75**, 119–133.

Torn M. S., Trumbore S. E., Chadwick O. A., Vitousek P. M. and Hendricks D. M. (1997) Mineral control of soil organic carbon storage and turnover. *Nature* **389**, 170–173.

Trenberth K. E. (2011) Changes in precipitation with climate change. *Clim. Res.* **47**, 123–138.

Vitousek P. M. and Chadwick O. A. (2013) Pedogenic thresholds and soil process domains in basalt-derived soils. *Ecosystems* **16**, 1379–1395.

von Lutzöw M., Kögel-Knabner I., Ekschmitt K., Matzner E., Guggenberger G., Marschner B. and Flessa H. (2006) Stabilization of organic matter in temperate soils: mechanisms and their relevance under different soil conditions - a review. *Eur. J. Soil Sci.* **57**, 426–445.

Wagai R., Kajiura M., Uchida M. and Asano M. (2018) Distinctive roles of two aggregate binding agents in allophanic andisols: young carbon and poorly-crystalline metal phases with old carbon. *Soil Systems* **2**, 29.

Wiesheu A. C., Brejcha R., Mueller C. W., Kogel-Knabner I., Elsner M., Niessner R. and Ivleva N. P. (2018) Stable-isotope Raman microspectroscopy for the analysis of soil organic matter. *Anal. Bioanal. Chem.* **410**, 923–931.

Wiesmeier M., Urbanski L., Hobley E., Lang B., von Lützow M., Marin-Spiotta E., van Wesemael B., Rabot E., Ließ M., Garcia-Franco N., Wollschläger U., Vogel H.-J. and Kögel-Knabner I. (2019) Soil organic carbon storage as a key function of soils - A review of drivers and indicators at various scales. *Geoderma* **333**, 149–162.

Wojdyr M. (2010) Fityk: a general-purpose peak fitting program. *J. Appl. Crystallogr.* **43**, 1126–1128.

Wolfe, E.W., Morris, J., 1996. Geologic map of the Island of Hawaii.

Associate editor: Jon Chorover